

AN ABSTRACT OF THE THESIS OF

Grant William Saltzgeber for the degree of Master of Science in Physics presented on September 19, 2012

Title: COMPARISON OF CARBON NANOTUBE AND GRAPHENE FIELD-EFFECT TRANSISTOR BIOSENSORS

Abstract approved: _____
Ethan D. Minot

Detection of biomolecules is important for the diagnosis and treatment of diseases. Low concentration detection, specific biomolecule detection, and point-of-care use are appealing characteristics for biosensors because of the possibility of early detection and quick results of specific biomolecules. Furthermore, inexpensive biosensors are appealing so that they are accessible to the general population. The biosensors in this study have the potential to satisfy these characteristics.

In this study graphene field-effect transistors (G-FET) were fabricated. Graphene was grown using chemical vapor deposition (CVD) and transferred to a silicon/silicon oxide substrate. The CVD method is the most scalable and cost-effective method of producing graphene for devices. Standard photolithography was used to pattern and then deposit metal electrodes. Two separate experiments were

conducted; one using electrostatic attraction to bind protein to the active area of the G-FET to detect the protein poly-L-lysine (PLL) and one using an aptamer modified G-FET to selectively detect the protein thrombin. Analyte was delivered using a homebuilt, pressure driven, microfluidic, mass flow system.

Both experiments showed a detection of the protein. The PLL experiment showed a clear change in the effective gate voltage of the G-FET. The thrombin experiment showed a change in the effective gate voltage that varied with differing concentrations of thrombin present. Furthermore, in the thrombin experiment by changing from a thrombin solution back to buffer the effective gate voltage was brought back to its original value. A competing protein was introduced and gave a signal comparable to the signal of a 10 times smaller concentration of thrombin. All of this shows that CVD grown graphene in a FET biosensor can be used for protein detection. Furthermore, the specific detection of thrombin suggests that aptamer modified G-FETs with CVD grown graphene can be used as a protein specific biosensor.

©Copyright by Grant William Saltzgeber

September 19, 2012

All Rights Reserved

COMPARISON OF CARBON NANOTUBE AND GRAPHENE FIELD-EFFECT
TRANSISTOR BIOSENSORS

by

Grant William Saltzgaber

A THESIS

submitted to

Oregon State University

in partial fulfillment of

the requirements for the

degree of

Master of Science

Presented September 19, 2012

Commencement June 2013

Master of Science thesis of Grant William Saltzgaber presented on
September 19, 2012

APPROVED:

Major Professor, representing Physics

Chair of the Department of Physics

Dean of the Graduate School

I understand that my thesis will be a part of the permanent collection of Oregon State University libraries. My signature below authorizes release of my thesis to any reader upon request.

Grant William Saltzgaber, Author

ACKNOWLEDGEMENTS

All of my accomplishments could have only happened because of the many people in my life. It is through these people's guidance, assistance, and love that all of this is possible. Family, friends and teachers are to thank for supporting me and pushing me to do my best.

I want to thank Ethan, for letting me be a member of this awesome group. Thank you for all of the stimulating talks and discussions. Your door was always open. You helped point me in the right direction throughout my entire graduate career. Thank you to Pete, because none of this would have been possible without your expertise in building such great devices. I want to thank Tal for all of your help. I can't express enough how I would have been totally lost in the lab without your help. Landon and Tristan, thank you guys for allowing me to continuously ask questions. I'm sure I got annoying. Thank you to all of the other Minot group members: Sophie, Jenna, Heather, Dan, and Hiral.

Thank you to all of my past professors from undergraduate and graduate school. You provided me with the knowledge to accomplish what I have. Thank you to my committee members, Dr. David McIntyre, Dr. Yun-Shik Lee, and Dr. Peter Greaney. A special thank you to Dr. Mike Larson, you provided so much direction for me during my undergraduate career. You went well above and beyond what you needed to. I want to thank Dr. Trecia Markes for all of the long chats, advising, and not only academic but life lessons.

I want to thank my family and friends. Mom and Dad, thanks for all you have done for me. I would not be the person I am without your parenting. I love you. To my brothers, Lee, Conrad, Scott, and Blake, I couldn't ask for a better group of guys to be my brothers and best friends. To my sister Gina thank you so much for always being there whenever I got down and pointing out the good things in life. To all of my in-laws present and future, I love having you as family.

Vanessa, thank you so much for all that you are. I know it has been very tough on us moving so many miles away from family, but we have always been there for each other through everything. This would never have been possible without you. I love you forever. Finally, I want to thank God for all of the blessings in my life.

TABLE OF CONTENTS

	<u>Page</u>
1. Introduction	1
1.1 Overview	1
1.2 Types of Commercial Biosensors	2
1.3 Field-Effect Transistor Biosensors	7
1.4 Graphene and Carbon Nanotube Basics	8
1.5 Graphene and Carbon Nanotube Field-Effect Transistor	13
2. Methods	20
2.1 Fabrication	20
2.2 Electrical Measurements	24
2.3 Microfluidic System	25
3. Results and Discussion	29
3.1 Selecting Devices for Biosensing	29
3.2 Noise Analysis	32
3.3 Poly-L-lysine Experiment	35
3.4 Thrombin Modified Graphene Device	39
4. Conclusion	47

LIST OF FIGURES

<u>Figure</u>	<u>Page</u>
Fig. 1.1 Schematic of surface plasmon resonance biosensor.....	3
Fig. 1.2 Schematic of enzyme-linked immunosorbent assay biosensor.....	4
Fig. 1.3 Schematic of quartz crystal microbalance biosensor.....	5
Fig. 1.4 Schematic of glucose biosensor.....	6
Fig. 1.5 Schematic of field-effect transistor biosensor.....	8
Fig. 1.6 Cartoon of graphene lattice.....	9
Fig. 1.7 Dispersion relation of graphene.....	13
Fig. 1.8 Geometry of a field-effect transistor.....	14
Fig. 1.9 Schematic of positive charge protein binding to substrate.....	15
Fig. 1.10 Schematic of protein binding to aptamer modified device.....	16
Fig. 1.11 Schematic of active area of a graphene device.....	17
Fig. 1.12 Predicted values of S_{input} for graphene and CNT device.....	19
Fig. 2.1 Schematic of device fabrication.....	21
Fig. 2.2 AFM image of CNTs.....	24
Fig. 2.3 Device circuit diagram.....	24
Fig. 2.4 Schematic of PDMS tunnel.....	26
Fig. 2.5 Schematic of flow system.....	27
Fig. 3.1 Typical transistor curve for G-FET devices used in this study.....	30
Fig. 3.2 Change in gate voltage changes Fermi level.....	31
Fig. 3.3 Consistency of devices.....	32

LIST OF FIGURES (Continued)

<u>Figure</u>	<u>Page</u>
Fig. 3.4 Current noise power spectra.....	33
Fig. 3.5 S_I data with curve fit.....	34
Fig. 3.6 Source-drain current for PLL experiment.....	36
Fig. 3.7 Change in effective gate voltage for PLL experiment.....	36
Fig. 3.8 Shift in transistor curve for PLL experiment.....	37
Fig. 3.9 Comparison of G-FET to CNT FET for PLL experiment.....	38
Fig. 3.10 Cartoon of aptamer on graphene.....	40
Fig. 3.11 AFM image of bare graphene and aptamer modified graphene...	40
Fig. 3.12 Device consistency for aptamer modified device.....	41
Fig. 3.13 Change in effective gate voltage for thrombin experiment.....	42
Fig. 3.14 Change in effective gate voltage vs. thrombin concentration.....	45
Fig. 3.15 Change in effective gate voltage for competing protein.....	46

COMPARISON OF CARBON NANOTUBE AND GRAPHENE FIELD-EFFECT TRANSISTOR BIOSENSORS

Chapter 1

Introduction

1.1 Overview

This chapter gives a general overview of biosensors. We review current commercially available biosensors and introduce field-effect transistor biosensors which are the focus of this research. Finally, a comparison between graphene and carbon nanotube field-effect transistor (FET) biosensors is made.

A biosensor is a device that detects the presence of biological molecules. The importance of biosensors is vast. The detection of low concentrations of specific biomarkers that relate to corresponding diseases is particularly important. Through detection of low concentrations, diseases can be diagnosed at an early stage resulting in early treatment and, in the case of deadly diseases, higher odds of survival.

Miniaturization of biosensors and real-time measurements have gathered interest because of the possibility of point-of-care use where a doctor and patient gets results during a consultation¹. This thesis focuses on a relatively new class of biosensor, based on nanoelectronic transistors, that promises both miniaturization and real-time measurements.

1.2 Types of Commercial Biosensors

There are a number of different biosensing techniques. Three of the more widely used categories are optical, piezoelectric, and electrochemical.² This thesis focuses on a new class of biosensor based on field effect transistors (FET). Before discussing FET sensors, we will review examples of existing widely-used biosensors.

Various types of optical biosensors exist. The most common are absorption, reflection (including SPR), fluorescence, chemiluminescence, and phosphorescence. Surface plasmon resonance (SPR) utilize surface plasmon polaritons, a special type of electromagnetic wave called a surface plasma wave, to investigate interactions between an analyte in solution and a biomolecular recognition element (see Figure 1.1). The basis of SPR is built around the fact that surface plasma waves are very sensitive to changes in index of refraction of dielectric mediums. Biomolecular recognition elements (BRE) are immobilized on a metal thin film, in many cases gold, then a flow of analyte solution is flushed over the top of the BREs and when the analyte binds to the BRE there is a slight change in the amount of light reflected from the metal. This is then the sensing mechanism.³ This technique provides label-free real time sensing of analyte activity. The main disadvantage to SPR is the expensive cost (commercial instruments cost more than \$100,000); hence it is primarily done in a lab setting.

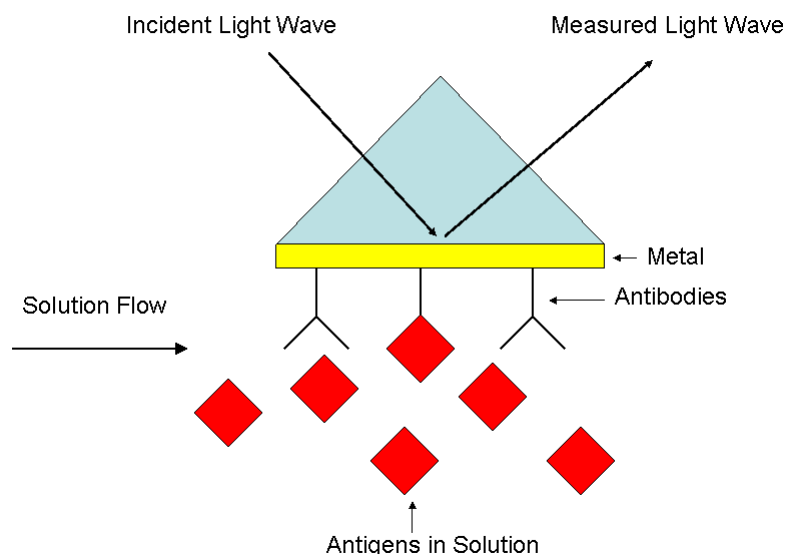


Fig. 1.1 A schematic of a Surface Plasmon Resonance (SPR) biosensor. A light wave is incident on a metal surface. The light wave couples to a surface plasmon polariton. The polariton is very sensitive to the dielectric of the metal and adjacent material which changes when antigens bind to antibodies that are immobilized on the metal. The change in polariton is then sensed through the reflected wave.

Fluorescence based biosensors, more commonly known as fluorescence immunoassay, use a fluorescent tag attached to some kind of molecule to detect the presence of proteins. One common technique is called enzyme-linked immunosorbent assay (ELISA) sandwich (see Figure 1.2). In this technique antibodies are immobilized on a surface then the antigens are introduced. The antigens that match up with the specific antibodies bind to the antibodies. Then antibodies that have a fluorescent tag connected to them are introduced and form an antibody sandwich around the antigen. If the sample fluoresces then one can assume that the antigen specific to the known antibody is present. This technique can get concentrations down to the subfemtomolar regime.⁴ Furthermore, ELISA can be used for single molecule detection.⁵ The major

disadvantage is that it is a label based technique as well as it takes several hours and a trained technician.

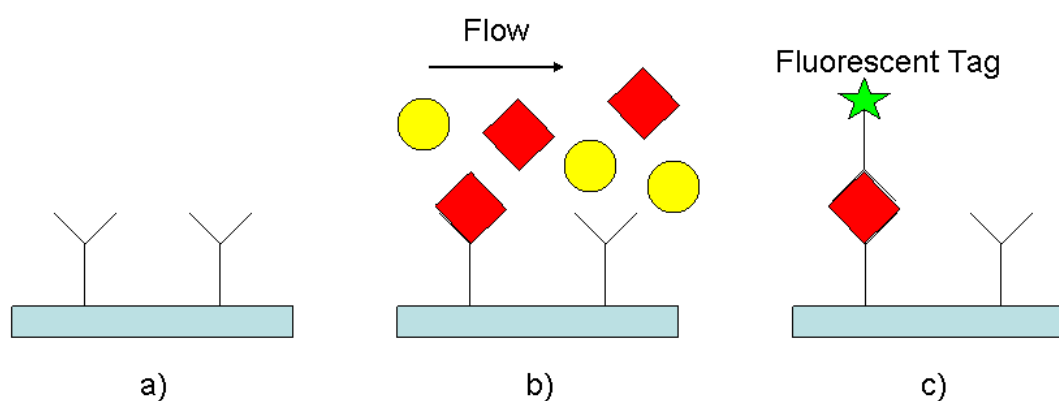


Fig. 1.2 Schematic of sandwich ELISA technique. a) Shows a surface functionalized with antigen specific to the red square antibody. b) Shows the introduction of antibodies and the specific antibody that coincides to the functionalized antigen binding to the antigen. c) Shows the introduction of fluorescently tagged antigens that are specific to the red square antibody. Hence if a sample fluoresces then one knows that the solution has the antibody that is specific to the antigens functionalized to the surface.

A piezoelectric biosensor that is generally used is the quartz crystal microbalance (QCM) shown in Figure 1.3. Quartz crystal microbalance biosensors utilize a piezoelectric material. Quartz is used as the piezoelectric material. Applying an alternating current to the quartz induces oscillations. When the mass adsorbed on the crystal is changed it changes the frequency of the oscillations which in turn changes the electrical signal associated with the oscillations. Changing the mass of the crystal is the basis of this sensor. In a basic model antibodies are immobilized on the sensor. Then antigens are introduced. When the antigens bind to the respective antibodies it changes the mass connected to the crystal and hence changes the

frequency of oscillations.^{6,7} Advantages of the QCM are the low cost of the device, along with the fact that it is a label-free sensor. Disadvantages are a requirement of high stability of circuit is necessary and extremely high phase stability.⁸

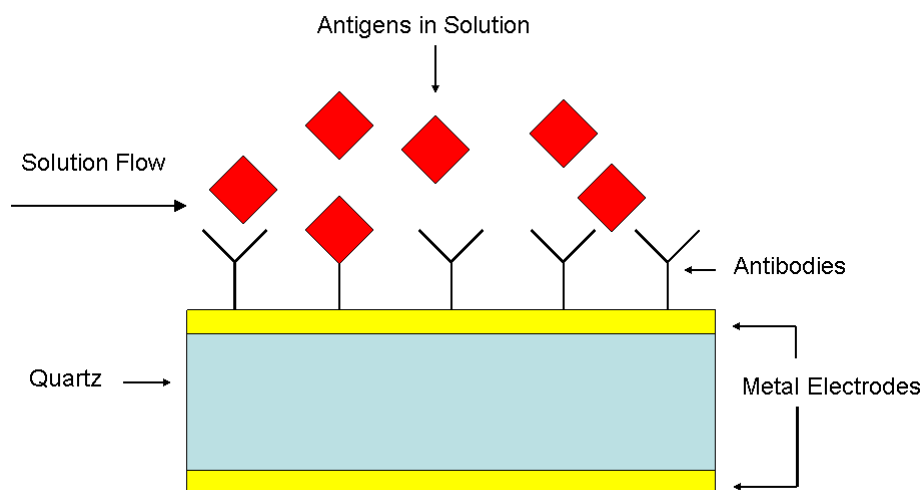
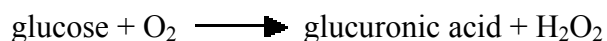


Fig. 1.3 Schematic of quartz crystal microbalance sensor. The metal electrodes apply a alternating current to the quartz causing oscillations. Antibodies are generally bound to the electrodes. When antigens bind to the antibodies it causes a mass change in the system which in turn causes a change in the frequency of the oscillations which is measured by the change in the electrical signals from the electrodes.

Glucose sensors are a type of electrochemical biosensor (see Figure 1.4). A platinum electrode is separated from glucose and glucose oxidase (GO) by a membrane that is permeable to O_2 . The GO is immobilized between this O_2 permeable membrane and another membrane that is permeable to O_2 and glucose. The glucose that enters the area with the GO is oxidized according to the reaction below.



Hence, the concentration of O_2 decreases as it moves up through the membrane to reach the cathode. This decrease in O_2 concentration is reflected as a decrease in current between the electrodes. Current is generated by the electrochemical reaction at the platinum electrode.



Hence, an electrical current can be used to monitor O_2 concentrations.^{1,9}

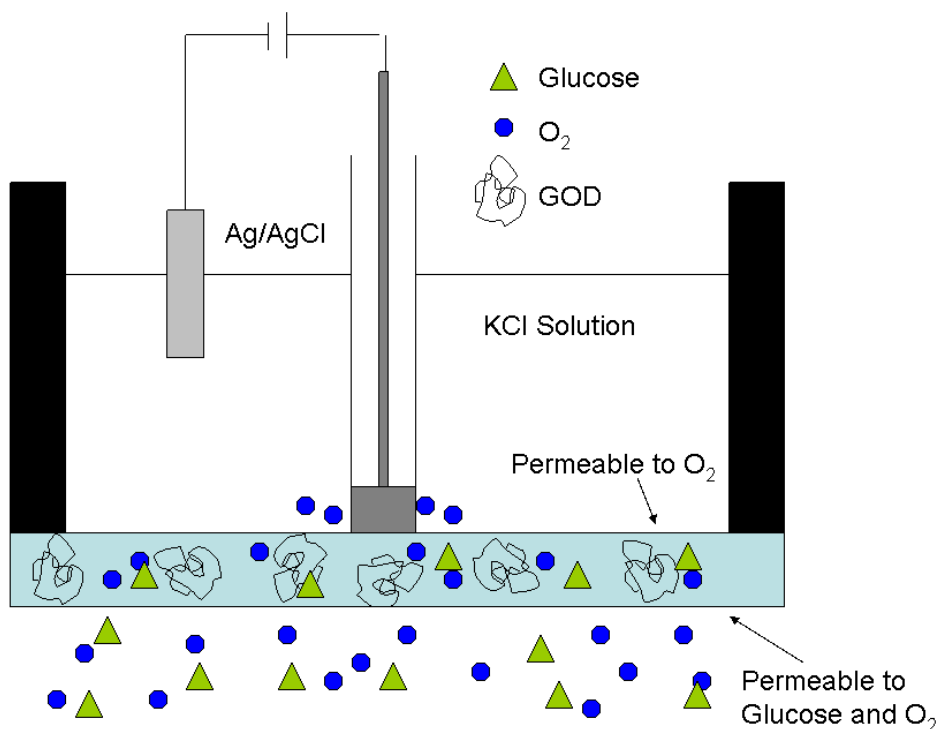


Fig. 1.4 Schematic of a glucose biosensor. Glucose and O_2 enter into the region with GOD where it goes through an oxidizing reaction. This reaction decreases the amount of O_2 that can get to the cathode hence changing the current. By this the amount of glucose in the solution can be found.

1.3 Field-Effect Transistor Biosensors

Field-effect transistor biosensors are currently in the research and development phase. A FET is made by placing metal electrodes on a semiconducting channel. When the electrostatic environment changes around the semiconductor it changes the conductance of the semiconductor. For example a protein that absorbs onto the FET will introduce a static charge, causing a change in conductance. The surface of these FET materials can be functionalized with a BRE such as antibodies and the transistor can be used as an antigen specific biosensor. A schematic of a generalized FET biosensor is shown in Figure 1.5. Operating principles will be discussed in more detail in the section 1.5. Many materials have been tested as the semiconducting channel in an FET biosensor. Among these materials graphene and carbon nanotubes (CNT) are both considered very promising. Graphene and CNT FET biosensors are the focus of this thesis.

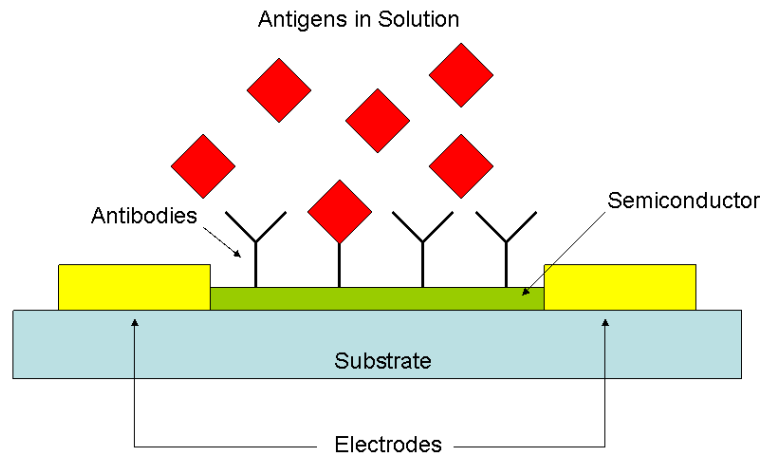


Fig. 1.5 Schematic of basic FET biosensor. Antibodies are immobilized on the semiconductor and then a solution of antigens is introduced. When an antigen binds to the antibodies the presence of the antigens changes the electric environment hence changing the conductance of the semiconductor.

1.4 Graphene and Carbon Nanotube Basics

Graphene is a two dimensional, single layer, lattice composed of carbon atoms. It has a honey comb structure where every carbon atom is bound to three other carbon atoms and six carbons make a hexagonal ring. The bond length between graphene and hence the distance between each carbon atom is 1.42 \AA .¹⁰ The unit cell with unit vectors can be seen in Figure 1.6. The rhombus is the unit cell and vectors \mathbf{a}_1 and \mathbf{a}_2 are the unit vectors. Each unit cell consists of two unique carbon atoms; atom A and atom B. In x, y coordinates, the two unit vectors can be expressed as

$$\begin{aligned} \mathbf{a}_1 &= \frac{\sqrt{3}}{2} a \cdot \hat{\mathbf{x}} + \frac{a}{2} \hat{\mathbf{y}} \\ \mathbf{a}_2 &= \frac{\sqrt{3}}{2} a \cdot \hat{\mathbf{x}} - \frac{a}{2} \hat{\mathbf{y}} \end{aligned} \quad (1.1)$$

where a is the lattice constant which equals $1.42 \text{ \AA} \times \sqrt{3} = 2.46 \text{ \AA}$.¹⁰

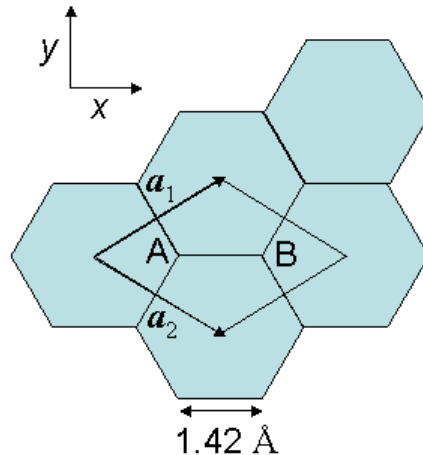


Fig. 1.6 Cartoon of graphene lattice. The rhombus shape is the unit cell of the lattice. Notice unit vectors \mathbf{a}_1 and \mathbf{a}_2 and atom spacing of 1.42 \AA . The unit cell spacing is 2.46 \AA . Each unit cell has two unique carbon atoms A and B.

The bonds between each carbon atom in the graphene lattice are composed of sp^2 hybrid orbitals. These orbitals occur when a $2s$ and two $2p$ orbitals hybridize. In Cartesian coordinates, if the x - y plane is chosen to be the plane that the lattice exists in, then the $2p_x$ and $2p_y$ orbitals are hybrid with the $2s$ orbital. The bonds that form between sp^2 orbitals in the carbon lattice are known as σ bonds. All σ bonds lie in the x - y plane.¹⁰ This leaves only the $2p_z$ orbitals. The $2p_z$ orbitals are perpendicular to the plane of the graphene lattice and are known as π orbitals.

A translational symmetry of unit cells makes up the lattice of graphene, because of this Bloch's theorem can be utilized.^{10,11,12} Bloch's theorem states that for any lattice with translational symmetry any wave function of that lattice should satisfy

$$\mathcal{T}\Psi = e^{ik \cdot a_j} \Psi \quad (1.2)$$

where \mathbf{T} is a translational operator along the lattice vector, \mathbf{a}_j and $j = 1, 2, \text{ or } 3$ for the three special dimensions for a three dimensional lattice, and \mathbf{k} is the wave vector. For graphene, j is just 1 or 2 because it is only a two dimensional lattice and these coincide to the two directions of the unit vectors in Figure 1.6 above. Furthermore, Ψ is the wave function of the lattice.^{10,11} A linear combination of plane waves is the most common form for Ψ . A function that satisfies equation 1.2 that is based on the atomic orbitals in the unit cell is

$$\Phi_s(\mathbf{k}, \mathbf{r}) = \frac{1}{\sqrt{N}} \sum_{\mathbf{R}} e^{i\mathbf{k} \cdot \mathbf{R}} \varphi_s(\mathbf{r} - \mathbf{R}) \quad (1.3)$$

where N is the number of unit cells in the lattice, \mathbf{R} is the position of the atom, s is the state the atom is in, φ is the atomic wavefunction in state s . Now if we assume only two atoms per unit cell, such is the case for graphene, we can rewrite equation 1.3 as

$$\Phi_s(\mathbf{k}, \mathbf{r}) = \frac{1}{\sqrt{N}} \sum_{\mathbf{R}_\alpha} e^{i\mathbf{k} \cdot \mathbf{R}_\alpha} \varphi_s(\mathbf{r} - \mathbf{R}_\alpha) \quad (1.4)$$

where α is A or B for the two atoms in the unit cell.

The Hamiltonian and overlap integral matrices are defined as

$$\mathbf{H}_{jj'}(\mathbf{k}) = \langle \Phi_j | \mathbf{H} | \Phi_{j'} \rangle, \quad \mathbf{S}_{jj'}(\mathbf{k}) = \langle \Phi_j | \Phi_{j'} \rangle \quad (1.5)$$

here j and j' are for the different atomic wavefunctions in each unit cell. The eigenvalues, E , which are found by solving the secular equation,

$$\det[\mathbf{H} - E\mathbf{S}] = 0 \quad (1.6)$$

provide the energy value as a function of \mathbf{k} value, also known as the dispersion relation. Substituting equations 1.4 and 1.5 into equation 1.6 will give the dispersion

relation of graphene. In graphene the most important energy bands are the π bands. They contribute the most to the electrical properties of graphene, so here we look only at the π bands. Furthermore, we use only the nearest neighbor interactions as an approximation. The Hamiltonian and overlap integral matrices are

$$\mathbf{H} = \begin{vmatrix} H_{AA} & H_{AB} \\ H_{BA} & H_{BB} \end{vmatrix}, \quad \mathbf{S} = \begin{vmatrix} S_{AA} & S_{AB} \\ S_{BA} & S_{BB} \end{vmatrix} \quad (1.7)$$

Each A atom is neighbored by three B atoms, the same is true for each B atom which is neighbored by three A atoms. Hence the only nearest neighbor interactions are between an A and B atom. Since atom A and atom B are both carbon atoms $H_{AA} = H_{BB}$ which is a constant, call it ϵ , and $S_{AA} = S_{BB} = 1$.

Now we look more closely at H_{AB} and S_{AB} .

$$H_{AB} = t(e^{k \cdot \mathbf{R}_1} + e^{k \cdot \mathbf{R}_2} + e^{k \cdot \mathbf{R}_3}) \quad (1.8)$$

\mathbf{R}_1 , \mathbf{R}_2 , and \mathbf{R}_3 are the three vectors that point from atom A to the three surrounding B atoms and t is what is known as the transfer integral.

$$\begin{aligned} \mathbf{R}_1 &= \frac{a}{\sqrt{3}} \hat{\mathbf{x}} \\ \mathbf{R}_2 &= -\frac{a}{2\sqrt{3}} \hat{\mathbf{x}} + \frac{a}{2} \hat{\mathbf{y}} \\ \mathbf{R}_3 &= -\frac{a}{2\sqrt{3}} \hat{\mathbf{x}} - \frac{a}{2} \hat{\mathbf{y}} \end{aligned} \quad (1.9)$$

Putting this into equation 1.8 gives

$$H_{AB} = t \left[e^{ik_x a / 3} + 2e^{-ik_x a / 2\sqrt{3}} \cos\left(\frac{k_y a}{2}\right) \right] \quad (1.10)$$

Since the Hamiltonian is a hermitian matrix, this implies that $H_{AB} = H_{BA}^*$. A very similar argument is made for S_{AB} and S_{BA} but in place of t is s , the overlap integral.

The secular equation can now be solved to find the energy of the π band.

Substituting equations 1.7 and 1.10 into equation 1.6 and solving for E results in

$$E(\mathbf{k}) = \frac{\varepsilon \pm t \sqrt{1 + 4 \cos\left(\frac{\sqrt{3}k_x a}{2}\right) \cos\left(\frac{k_y a}{2}\right) + 4 \cos^2\left(\frac{k_y a}{2}\right)}}{1 \pm s \sqrt{1 + 4 \cos\left(\frac{\sqrt{3}k_x a}{2}\right) \cos\left(\frac{k_y a}{2}\right) + 4 \cos^2\left(\frac{k_y a}{2}\right)}} \quad (1.11)$$

This is the energy of the π bands as a function of \mathbf{k} for graphene. In Figure 1.7, E is plotted as a function of \mathbf{k} . Notice how there are two bands in the plot. These coincide to the plus and minus in equation 1.11 and are known as the π and π^* or binding and anti-binding bands respectively. The Fermi energy is located at $E = 0$. One of the more interesting characteristics is at the point where the π and π^* bands touch. This point is known as the Dirac-Point and gives graphene its zero band gap semiconductor properties.

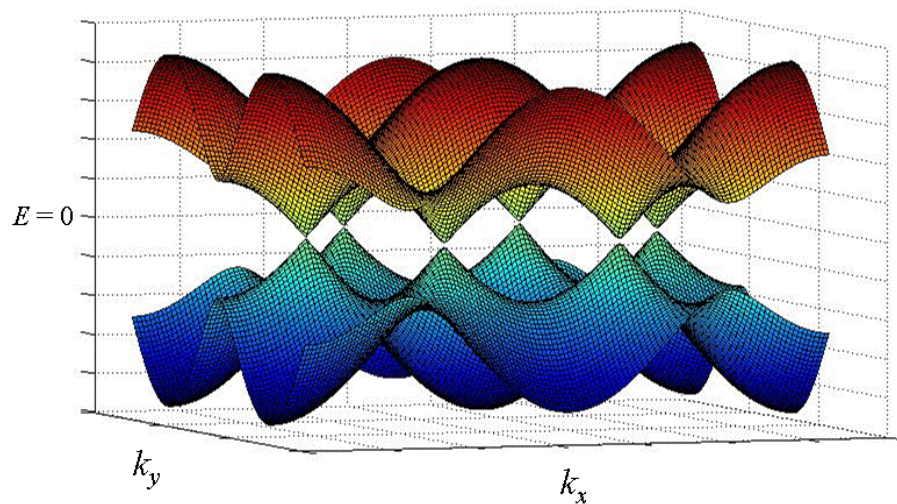


Fig. 1.7 Dispersion relation of graphene. The valence and conduction bands do not cross but touch at what is called the Dirac point. This gives graphene its zero band gap semiconductor characteristics.

Carbon nanotubes are very similar to graphene. They are just a graphene sheet rolled into a cylindrical geometry. Hence, a very similar treatment can be used on CNTs as on graphene. The biggest difference is that now the x direction must have a continuous boundary condition connecting the two edges of the graphene sheet that was rolled to form the CNT. This makes it possible for only one k value in the x direction. Carbon nanotubes can then be treated as a one dimensional entity. Furthermore, this introduces a band gap in the dispersion relation of CNTs.

1.5 Graphene and Carbon Nanotube Field-Effect Transistors

1.5.1 Basic Structure of Graphene and Carbon Nanotube Field-Effect Transistors

Graphene and CNT FET have similar structures. Metal electrodes, known as the source and drain electrodes respectively, are connected to either end of the

nanomaterial. This material between the source-drain electrodes is the transistor channel. A voltage difference is applied to the source-drain electrodes causing a current through the graphene/CNT. Another voltage, known as the gate voltage, is then applied to the system either through a back gate or through a reference electrode in solution. This gate voltage changes the electrostatic environment of the graphene/CNT causing a change in the Fermi level, which is reflected in the conductance of the CNT. Carbon nanotube transistors often have multiple CNTs in the transistor channel. For graphene transistors there is typically a single sheet of graphene connecting between the source-drain electrodes.

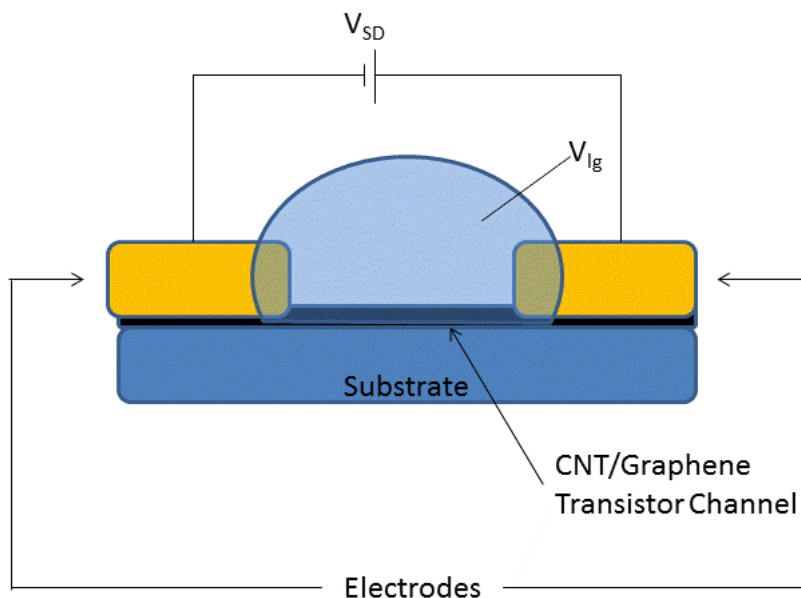


Fig. 1.8 Basic geometry of a field-effect transistor. The CNT/Graphene lays on a substrate with two electrodes, the source and the drain, in contact on either end. There is a voltage difference between the source and drain electrode and a reference electrode applies a liquid gate voltage.

1.5.2 Basics on how Field-Effect Transistors work/binding mechanism for proteins

The conductance of a field-effect-transistor (FET) changes with a change in electrostatic environment. When a charged protein is brought within close proximity to a carbon nanotube (CNT) or sheet of graphene in a FET, the electrostatic environment is changed which in turn changes the conductance of the FET. Binding the protein to the regions close to the CNT/graphene leads to the collection of protein close to the sensitive areas of the biosensor. This allows for the detection of low concentrations of proteins. The signal from a given surface coverage of protein can be expressed as ΔV_g , the effective change in gate voltage.

There are different ways to bind proteins to the sensitive regions of a FET. In this study two techniques were utilized. The first technique was by electrostatic attraction. When the substrate of a FET is charged it is possible to bind a protein of opposite charge to the substrate¹³ (see Figure 1.9).

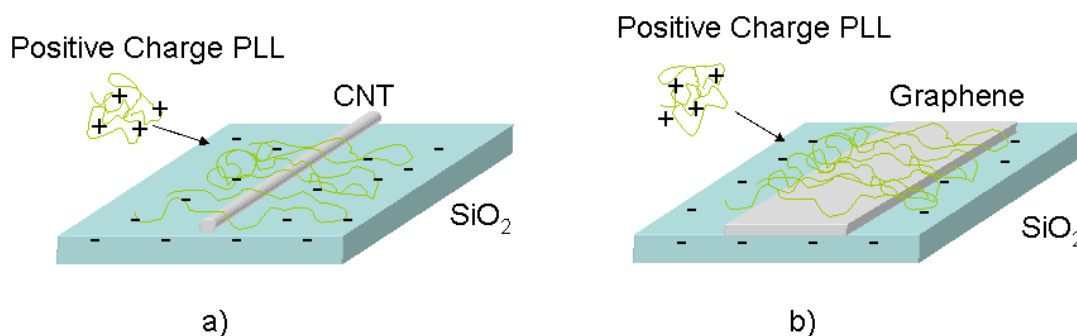


Fig. 1.9 Schematic of positive proteins, in this study Poly-L-Lysine (PLL), binding to the negative silicon oxide substrate. When this binding happens the presence of the positive charges from the PLL changes the conductivity of the semiconducting CNTs or graphene.

The second technique was by use of single strand Deoxyribonucleic acid (ss-DNA) aptamers which bind to a specific protein. Aptamers can be attached to the surface of CNTs and graphene.¹⁴ When the protein binds to the aptamer it is immobilized near the sensitive region of the FET (see Figure 1.10). With this technique it is possible to have protein specific biosensors.

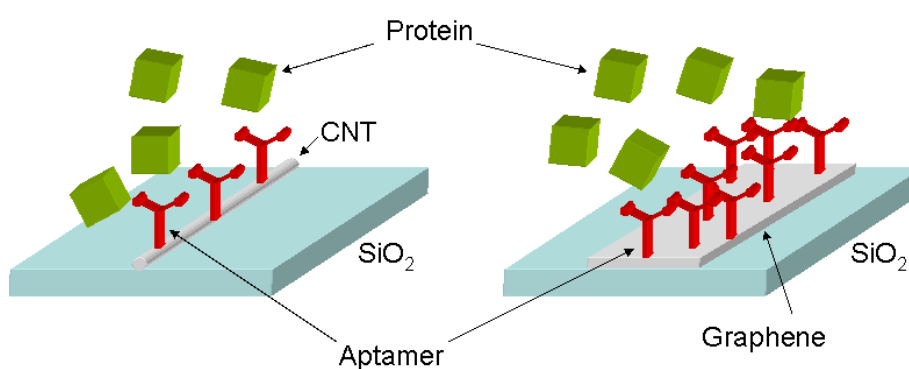


Fig. 1.10 Schematic of aptamer modified graphene/CNT biosensors. The aptamer is specific to a certain protein. When that protein binds to the aptamer there is a change in the electrostatic environment near the graphene/CNT changing the conductivity.

1.5.3 Graphene vs. Carbon Nanotube Field Effect Transistors

Together with any electrical signal there is noise. Reducing the noise level in a detection instrument will in turn enhance the capabilities of that instrument. This section discusses noise in carbon nanotube and graphene field-effect transistors. A brief analysis and overview of the advantages and disadvantages of each material is considered.

It was shown by Männick, *et. al.* that S_{input} , the noise-power spectral density measured in V^2/Hz (effective fluctuations on gate voltage) scales with the inverse of the length of a single CNT in a liquid gated CNT FET. Männick also showed that the

noise spectra for current fluctuations can be modeled as, $S_I = S_{\text{input}}(dI/dV_{\text{lg}})^2$ for where I is the source drain current and V_{lg} is the liquid gate voltage (see Figure 1.8). This noise parameter, S_{input} , was experimentally found to be $0.54 [\text{mV}^2\mu\text{m}/\text{Hz}]/L$ where L is the length of the CNT.¹⁵

Noise in graphene FETs has also been experimentally studied. It was shown that $S_{\text{input}} = \xi/\text{Area}$, where $\xi = 0.11 \mu\text{m}^2\text{mV}^2/\text{Hz}$ was experimentally found for single layer graphene.¹⁶

From the work of Mannik and Heller we can compare the predicted noise levels for CNT FETs and G-FETs. If the device dimensions are width w by length l as in Figure 1.11, then the area of the device is wl . Assuming that S_{input} for CNTs depends on the total length of CNTs present in the transistor channel, then S_{input} is

$$S_{\text{input}} = \frac{.54}{\sigma_{\text{CNT}} wl} (\text{mV}^2\mu\text{m}/\text{Hz}) \quad (1.12)$$

where σ_{CNT} is the CNT density, the number of CNTs per unit length in the x direction.

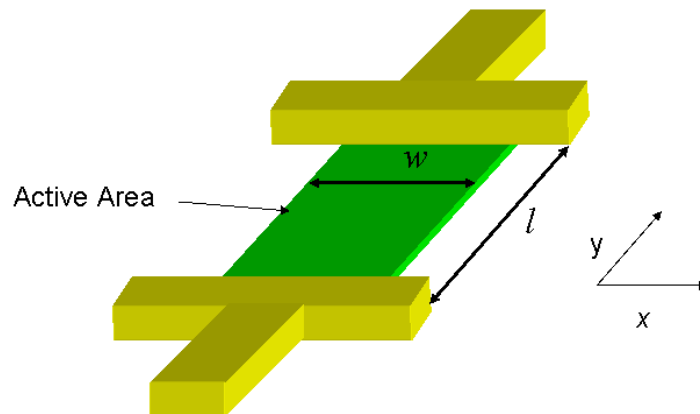


Fig. 1.11 Schematic of active area of a graphene device.

Then total length L of all the CNTs in the channel is simply, $wl\sigma_{CNT}$. For a graphene device with the same device dimensions, wl , S_{input} is

$$S_{input} = \frac{.11}{wl} (\text{mV}^2\mu\text{m}^2/\text{Hz}) \quad (1.13)$$

By setting the respective S_{input} values equal, we calculated a critical density.

$$\frac{.54}{\sigma_{CNT}^* wl} (\text{mV}^2\mu\text{m}/\text{Hz}) = \frac{.11}{wl} (\text{mV}^2\mu\text{m}^2/\text{Hz}) \quad (1.14)$$

Solving for σ_{CNT}^* reveals a density of 4.91 CNTs/ μm or about 5 CNTs/ μm is needed for GFETs and CNT FETS to have equal S_{input} . Notice how the dependence of the width and length of the active area divides out hence σ_{CNT}^* has no w or l dependence. Figure 1.12 shows S_{input} for both CNT and G-FET devices with $w = 5\mu\text{m}$, $l = 5\mu\text{m}$.

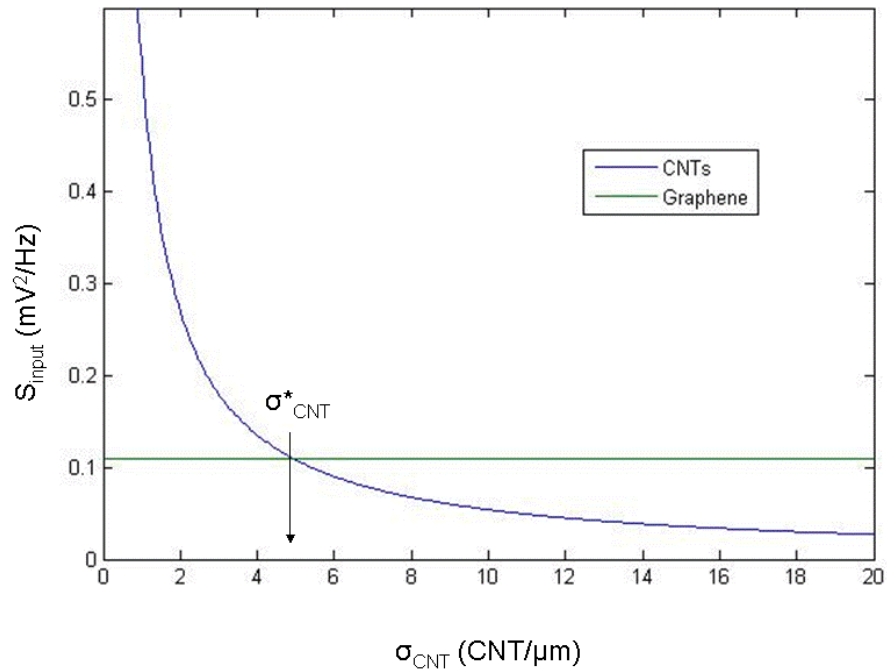


Fig. 1.12 Plot of S_{input} for graphene and CNT devices. Blue line is for CNT, green line is for graphene. At a CNT density of about 5 CNT/ μm S_{input} for graphene is equal to CNT devices. In region 1 graphene is the better choice where in region 2 CNTs are the better choice for FET devices.

Unfortunately, it is not easy to grow aligned CNTs at densities $\sigma_{\text{CNT}} > 5$

CNTs/ μm . In this work the highest level of CNT density growth was on the order of 3-4 CNTs/ μm . It is even harder to make low-noise contacts to 100% of CNTs.

Additionally, it is currently impossible to grow 100% semiconducting CNTs. Hence, we conclude that graphene is currently a better choice for FET biosensors, and we cannot do better than the GFET noise floor, for a given device area.

Chapter 2

Methods

This chapter discusses the fabrication of both CNT and graphene FETs. It continues with a general overview of how electrical measurements were taken. Finally, a description of the experimental set-up including the microfluidic system used for analyte delivery is presented. For a more in-depth description of G-FET fabrication see Pete Wojcik's 2012 master's thesis.

2.1 Fabrication

The graphene was chemical vapor deposition (CVD) grown on copper sheets. The copper sheet with graphene was then cut into two centimeter by two centimeter square pieces for transfer. The side of the square pieces with graphene had polymethyl methacrylate (PMMA) in a solution of Anisole spun coat onto it and was then placed in a copper etch bath. After the copper etch bath the samples of graphene on PMMA were then placed in three separate deionized water baths for 30 minutes and then a final deionized water bath for a minimum of 12 hours. The graphene on PMMA samples were then removed from the water bath with a clean silicon chip with a layer of 300 nm thick silicon oxide on the surface and alignment marks. Drying the graphene after the final transfer to the Si/SiO₂ was done in a gentle fashion with a middle to edge fashion to help the graphene adhere to the surface using high purity nitrogen gas. The samples were then placed in a 30°C furnace for 4 hours to further

adhere the graphene to the surface. The PMMA was then removed from the graphene by placing the sample in a one inch furnace at 350°C for 4 hours.

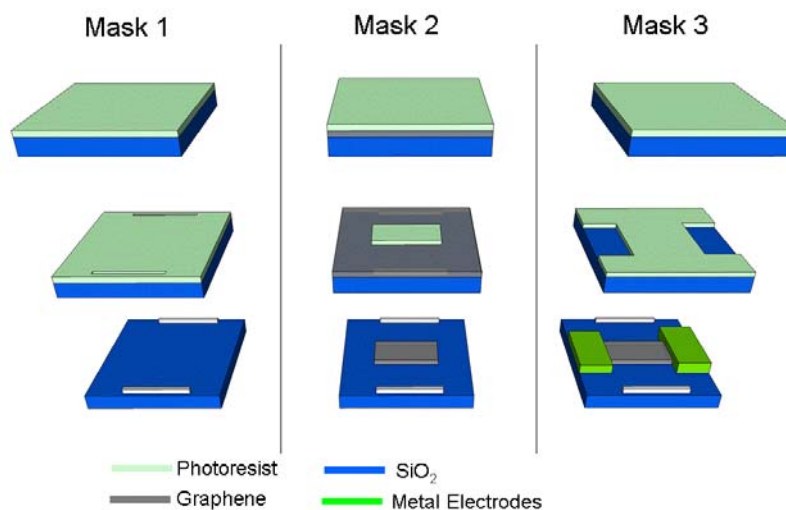


Fig. 2.1 Fabrication process for patterning alignment marks, graphene ribbons, and metal electrodes on surface of chip. A three mask photolithography process was used to make devices. The graphene transfer was done after the patterning the alignment marks from the first mask. Image taken from Pete Wojcik 2012 thesis.

Alignment marks were used during the fabrication of devices. This was to ensure that the graphene ribbons would be properly aligned in electrode gaps. The Alignment marks were the first step in the fabrication process and were patterned using standard photolithography and a metal deposition. The samples were spin coated with LOR3A at 4000 rpm for 45 seconds then baked on a hot plate for 4 minutes at 190°C. This under layer aids in the process of metal lift off. S1813 photoresist was then spun coated at 4000 rpm for 30 seconds and baked on a hot plate for 90 seconds at 190°C. The samples were then exposed in a contact aligner for 4.5 seconds. The samples were developed in AZ-726 for 90 seconds and rinsed in a short DI bath. 20 nm of chrome was deposited using an electron beam (e-beam) metal evaporator. The

samples were then placed in PG remover for at least 12 hours at 70°C to remove any photoresist and excess metal.

To get ribbons in the gap between electrodes, the graphene had to be etched away from all areas except in the wanted ribbon areas. Standard photolithography was again used but a layer of P20 primer was spun coat at 4000 rpm for 30 seconds and then the S1813 photoresist was put down on top and process in the same manner as stated above. After developing in AZ-726 for 90 seconds and rinsing in a short DI bath, the samples were placed in an O₂ plasma etcher to remove all the graphene except the wanted ribbons.

The last step in the fabrication process is the deposition of the metal electrodes. The photolithography and metal deposition procedures for this step are identical to the alignment mark procedure except for the type of mask and metal used. An appropriate mask designed for electrodes was used in the contact aligner. During the e-beam metal deposition a 1.5 nm layer of chrome was deposited first and acted as the sticking layer. 30 nm of gold was then deposited on top of the chrome to create the bulk of the metal electrodes.

The CNT devices were fabricated on quartz chips. The quartz chips were first cleaned with acetone, isopropyl alcohol (IPA), deionized water (DI), and annealed in open air at 900°C for one hour. Then catalyst was applied through a spin coat process. A solution of iron nitrate nonahydrate (1.62g) and molybdenum dioxide bis(acetylacetonate)(0.65g) in methanol (40 mL) was mixed in S1813 photoresist at a ratio of 1:100 iron solution to photoresist. The iron in the solution acted as the catalyst for

CNT growth. Initially, P-20 was spun coat at 4000 RPM for 30 sec. Then the photoresist iron solution was spun coat at 4000 RPM for 30 sec. and then baked on a hot plate at 115 °C for 90 sec. The chip was then exposed in a contact aligner, the same aligner that was used in the graphene fabrication. The mask used left parallel lines of iron catalyst and photoresist that were 10 μm thick and spaced 50 μm apart. The chip was then annealed at 800°C for 10 minutes to burn off the photoresist and leave behind catalyst.

Carbon nanotubes were grown by CVD in a one inch diameter tube furnace. The process started with a 10 minute open air anneal at 800°C. All flow lines of gases used were then purged at less than 300°C for 2 minutes. A hydrogen anneal was then done with a flow rate of 0.45 SLM at 800°C for 15 minutes. For the CNT growth process the tube was sealed and then a mixture of 0.45 SLM Hydrogen, 0.15 SLM argon bubbled through methanol, and 0.3 SLM argon bubbled through ethanol. This was done at 900°C for 15 minutes. The furnace was then cooled under argon flow. This produced CNTs with diameters of approximately 1-3 nm all aligned. Growing on the quartz substrate was the key to obtaining aligned CNT growth. Figure 2.2 shows the growth results. Notice the growth density of approximately three CNTs per μm .

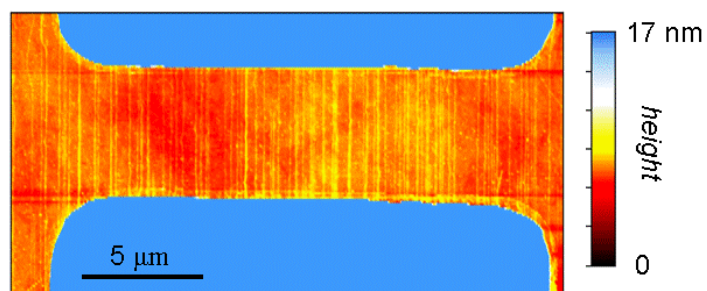


Fig. 2.2 AFM image of CNTs with electrodes. The vertical parallel lines are the CNTs in the transistor channel. The density is 3 CNTs/ μm .

Electrodes were then patterned onto the chip in the same manner as with the graphene devices. Then another photolithography step was done to cover the electrodes with photoresist. The chip was then put in an O_2 plasma etcher to remove all the CNTs except the ones in the transistor channels.

2.2 Electrical Measurements

Figure 2.3 shows the circuit diagram of the devices. A current preamplifier,

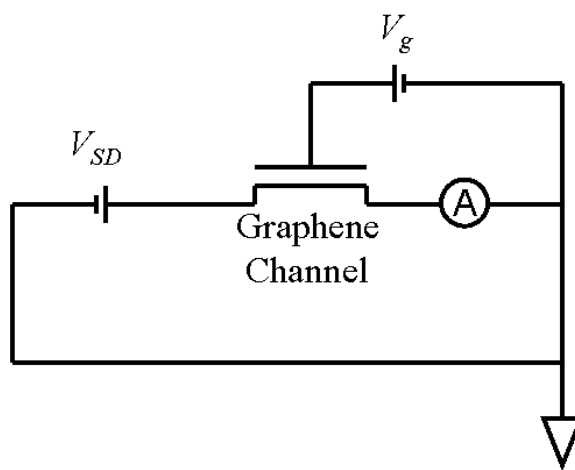


Fig. 2.3 Circuit diagram of devices.

Stanford Research Systems (SR570), provided the source drain voltage of 25 mV. The same preamplifier was also used to measure the current of the circuit, which was converted to a voltage and sent to a National Instruments DAQ (NI USB 6251) analog to digital converter. The basis of the 25 mV choice was that it coincides to k_bT for an electron at room temperature. Two micromanipulator probe needles were used to contact gold pads on the chip which completed the circuit with the preamplifier. The reference electrode gate voltage was set by a voltage source (Yokakawa GS200 DC). The current preamplifier has an adjustable filter. For measurements the preamplifier was set to high band-width at 3 kHz frequency filter. This was chosen so that noise measurements could be collected. All measurements were taken inside a dark box that also served as a Faraday cage. When taking electrical measurements it was important to reduce all noise from extraneous sources and have a common ground. The probe needles are connected to coaxial cable with shielding that shares a common ground with the Faraday cage and preamplifier that was providing the source drain voltage. Electrical noise in the sensor circuit was reduced by having the preamplifier running on battery power.

2.3 Microfluidic System

A microfluidic system was devised to deliver analyte solution to the active area of the biosensor. A polydimethylsiloxane (PDMS) stamp with a 100 μm by 200 μm trench was placed on the chip. The trench was situated so that it ran above the active areas making a tunnel for solution to flow through and analyte to have access to the

sensor. Before use the PDMS stamp went through a cleaning which involved a 30 minute soak in hexane then a 30 minute soak in IPA and finally was sonicated for 5 minutes in ethanol. The mold for creating a PDMS flow channel is made from 100 μm thick photoresist (SU8 3050 from Microchem). The photoresist mold is patterned in a contact aligner and then developed following the manufacturer's guidelines. PDMS is mixed (10:1 ratio of resin to hardener) and then poured on top of the photoresist mold. The PDMS is cured overnight at room temperature and then removed from the mold. The resulting flow channels are 100 μm tall and 200 μm wide.

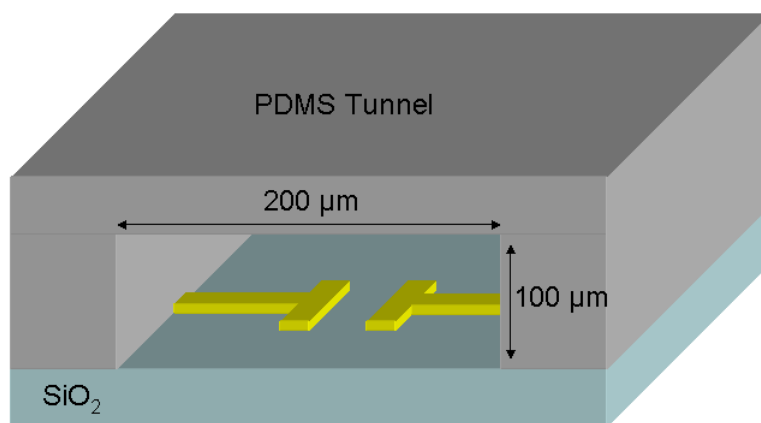


Fig. 2.4 Schematic of PDMS tunnel above device in microfluidic system.

After the PDMS stamp was made it had to be pressed to the chip and make a water tight seal for the fluid experiment. To seal the PDMS stamp to the chip an acrylic flow cell was used to clamp down and seal the PDMS stamp to the chip. This made a sandwich of the chip, PDMS stamp, and flow cell with the PDMS stamp tightly fit between the flow cell and chip. The flow cell is equipped with the intake and output of

fluid for the system. Fluid would flow into the flow cell, down into the PDMS stamp, through the tunnel with access to the sensor, back up through the PDMS stamp, back into the flow cell, and discarded through an output line into a waste container. The input and output lines of the flow cell were 0.0127 cm inner diameter tubing. Two types of systems were used to deliver pressure to the flow lines. One type was a syringe pump and the other was a home made pressure system which utilized high purity nitrogen and pressure regulators sealed off to the system to provide the force to stimulate the fluid flow.

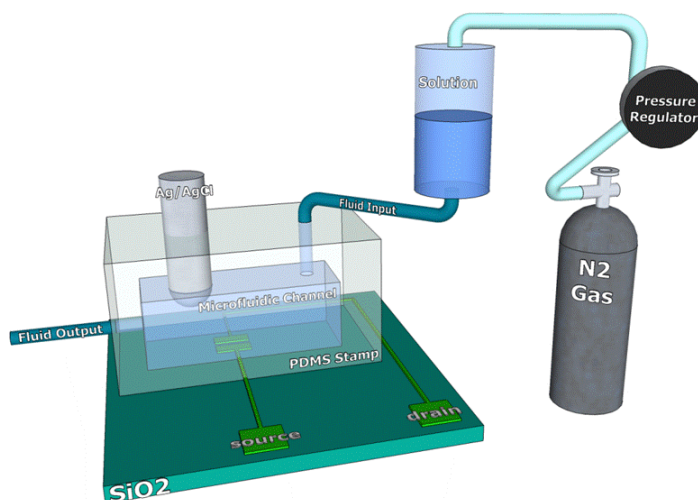


Fig. 2.5 Schematic of experimental set-up of flow system. Image taken from Pete Wojcik's master's thesis 2012.

The flow cell was also equipped with a reference electrode. The reference electrode was a Ag/AgCl electrode which was in contact with the fluid. It could be used to generate transistor curves as well as set the liquid gate for experiments. Typical transistor curves were obtained by measuring the current of the device while the gate voltage was swept from -500 mV to 400 mV. This range was sufficient to get

the on/off states for the transistor as well as identify the Dirac Point in the graphene transistors. A typical transistor curve can be seen in Figure 3.1. The liquid gate values for sensing experiments were set according to locations in the transistor curve where the magnitude of slope of the curve was greatest. Faradaic currents are monitored and kept at a minimum to prevent a false signal.

Chapter 3

Results and Discussion

This chapter discusses the results from the PLL and thrombin biosensing experiments. First, device selection and device characteristics are discussed. Then the PLL biosensing results are presented and analysis given. Finally, the thrombin biosensing results are discussed and analyzed.

3.1 Selecting devices for biosensing

The fabrication process gives some variation between devices. At the beginning of each experiment, devices were checked to ensure desirable characteristics. To do this the graphene FET was placed under a polydimethylsiloxane (PDMS) stamp with the microfluidic tunnel as described in Chapter 2. For PLL experiments a phosphate buffered saline solution at pH 7.2 was delivered through the microfluidic channel. For thrombin experiments a 2-morpholinoethanesulfonic acid (MES) buffer at pH 7.2 was delivered through the microfluidic channel. Noise measurements and transistor curves were taken with just the buffer present. Figure 3.1 shows a typical transistor curve for the G-FET devices used. It has a clear Dirac point that is near 0 V, this indicates that very little doping is present in the graphene. Also, the ratio of maximum over minimum current values was approximately 4.

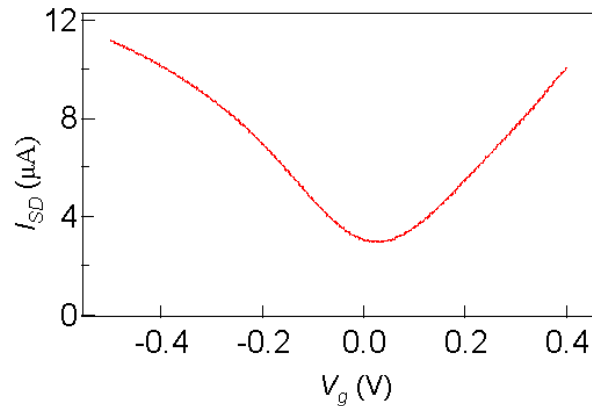


Fig. 3.1 Typical transistor curve for G-FET devices used in this study. A clear Dirac point is present that is close to a gate voltage of 0 V indicating very little doping. When the gate voltage is on the negative side of the Dirac point the carriers are p-type, when it is on the positive the carriers are n-type.

This minimum point in a transistor curve for a G-FET is called the Dirac point. This is the location where the Fermi level of electrons is right where the conduction band and valence band meet in the dispersion relation (see Figure 1.7). When the gate voltage is set on the negative side of the Dirac point the Fermi level lies at a point where the carriers in the system are holes because the Fermi level is shifted down in energy into the valence band. When the gate voltage is set on the positive side of the Dirac point the Fermi level is shifted up in energy to the conduction band and the carriers are electrons.

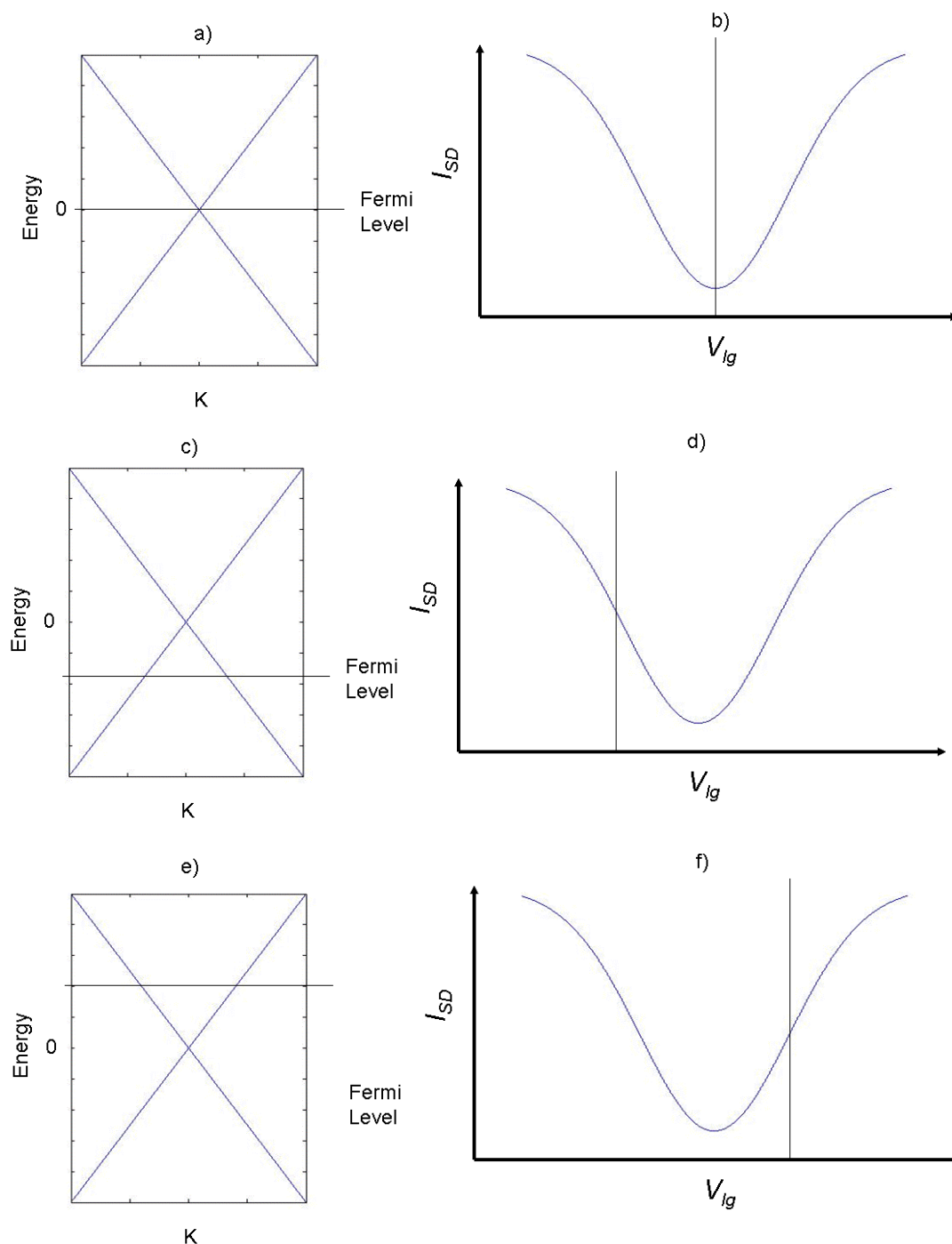


Fig. 3.2 Cartoon of how the change in gate voltage changes the Fermi level of the system. The vertical line in b), d), and f) shows different regions where the gate voltage can be, a), c), and e) show the corresponding Fermi level in the band structure.

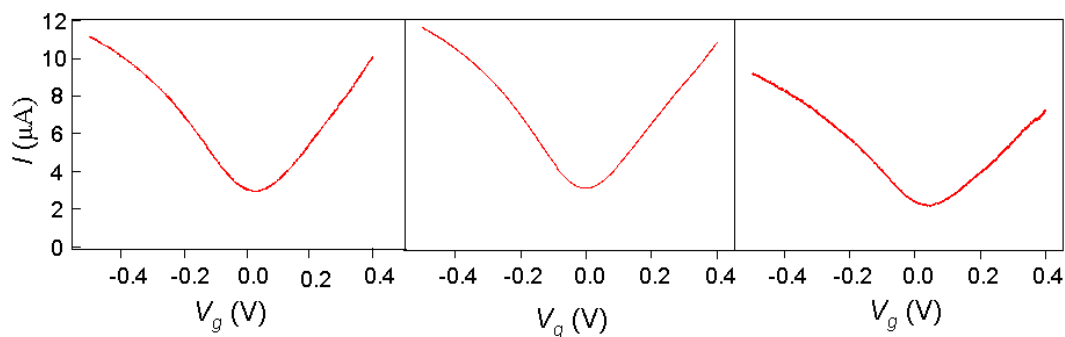


Fig. 3.3 Transistor curves from three different devices showing the consistency of devices built.

Figure 3.3 shows transistor curves from three different devices with bare graphene. The transistor curve is consistent from device to device. This consistency is important when considering mass production of these devices.

3.2 Noise Analysis

Before any protein was introduced measurements were taken to analyze the noise present in each device. In Figure 3.4 the current noise power spectra is plotted at two different gate voltages for one device.

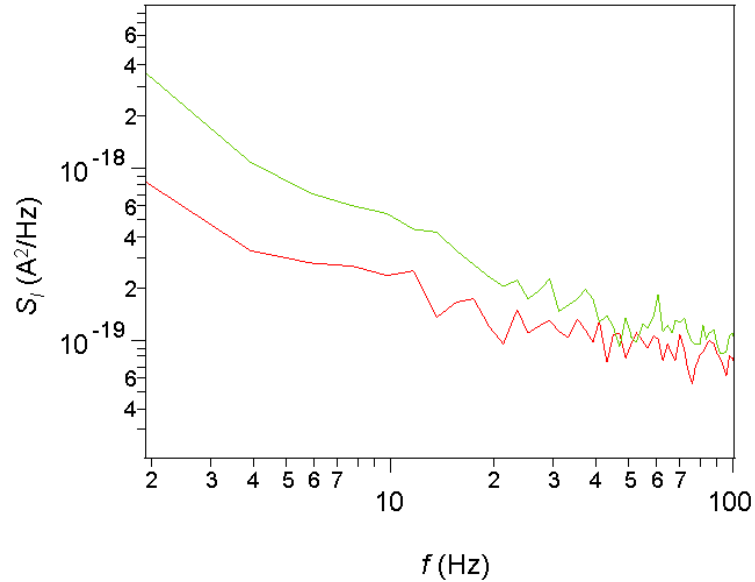


Fig. 3.4 Current noise power spectra. Red line is at gate voltage 50 mV which is the Dirac point. Green line is at gate voltage -100 mV. Data was filtered by hardware at 3 kHz. Sampling was done at 2 kHz.

The green is at gate voltage of -100 mV and the red is at the Dirac point at gate voltage 50 mV. There is approximate $1/f$ noise dependence. Figure 3.5 shows the extracted S_I values at 10 Hz for different gate voltages. The solid red dots are the real data. The solid blue line is a fit using the augmented charge noise model $S_I = S_{input} (dI_{SD}/dV_{lg})^2 + \alpha I_{SD}^4$ where S_{input} and α are the fit parameters.¹⁶

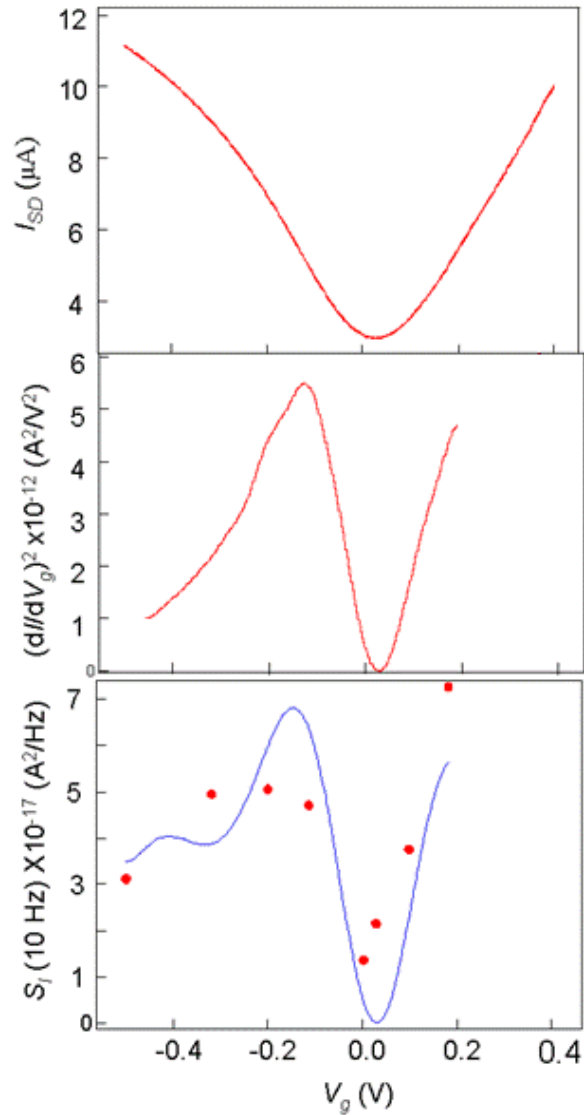


Fig. 3.5 Top is the transistor curve. The Middle graph is $(dI/dV_g)^2$. Bottom is S_I data at 10 Hz (red dots) and the curve fit using the augmented model (ref Heller).

The S_{input} value found was $1.2 \times 10^{-9} \text{ V}^2/\text{Hz}$ which is within a factor of two of the value of $.7 \times 10^{-9}$ found by Heller et. al. for mechanically exfoliated graphene.

3.3 Poly-L-lysine Experiment

Two types of biosensing experiments were performed, PLL and thrombin. In this section the PLL experiment will be discussed.

After all the noise measurements were taken, a transistor curve was measured. The gate sweep for this transistor curve was from -500 mV to 400 mV at a rate of 4 $\mu\text{V}/\text{sec}$. The idea for the PLL experiment is that the PLL will bind to the SiO_2 surface (see Figure 1.9). Poly-L-lysine has one positive charge per monomer at neutral pH giving it a net positive charge of $170e$. It's molecular weight is 25 kDa and has a diffusion constant of $4 \times 10^{-13} \text{ m}^2 \text{ s}^{-1}$. It has a strong affinity to bind to the negatively charged SiO_2 substrate of the devices. All PLL experiments were carried out in PBS buffer pH=7.2 with NaCl concentration of 137 mM, KCl concentration of 2.7 mM, and phosphate buffer of 10 mM. The SiO_2 surface has a charge density of approximately $-2.5 \mu\text{C cm}^{-2}$ at these pH and salt levels.¹⁷

In this experiment the reference electrode voltage was set at -125 mV. Then a solution of 44 nM PLL mixed in the PBS buffer at 7.2 pH was introduced into the system. The flow rate for this solution was approximately 2.5 mL/hour. Figure 3.5 shows I_{SD} vs time data. When PLL binds to the substrate near the graphene the source-drain current changes.

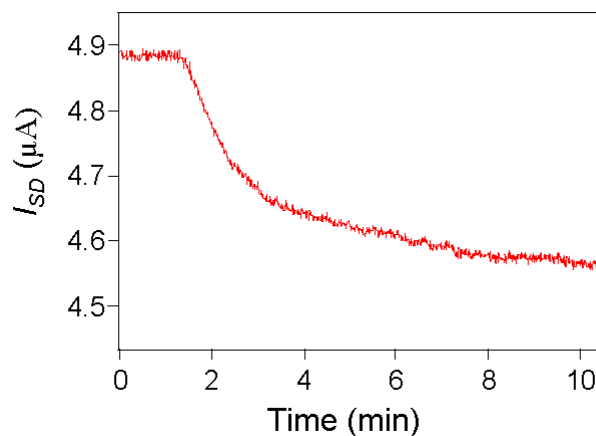


Fig. 3.6 Real time data of source-drain current during PLL experiment. Data was filtered by hardware at 3 kHz. Sampling was done at 2 Hz.

To analyze this real time data, $I(t)$ is converted to $\Delta V_g(t)$, the effective change in gate voltage. To convert $I(t)$ from to $\Delta V_g(t)$ we use dI/dV_g measured from the transistor curve Figure 3.1.

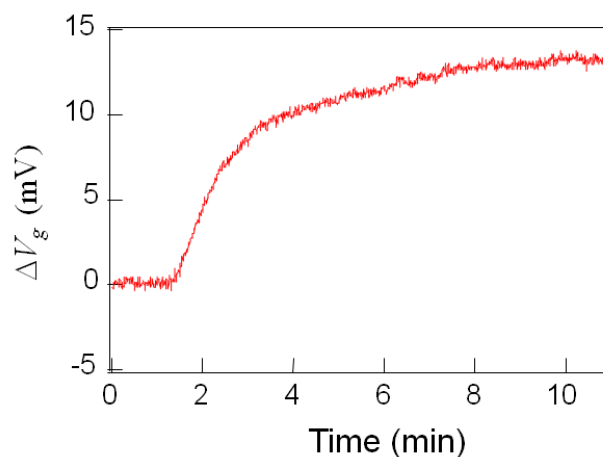


Fig. 3.7 Time data of PLL experiment PLL concentration of 44 nM added at $t = 1$ min. The effective gate voltage, ΔV_g , changes as PLL binds to the surface of the sensor. Notice the different regions of change. From 2 to 2.5 min the change in ΔV_g is very linear and then from there on it is non-linear as the surface saturates with PLL.

Looking at Figure 3.7 a few things are noticed. At time = 0 min, there is only a flow of PBS buffer. This gives the flat line when no protein is on the surface. The protein is introduced at about time = 1 min. There is a small lag between when protein flow is first started and when it gets to the sensor. This is due to lag in the line from the syringe to the chip. A little before 2 mins into the experiment ΔV_g begins to change. At first it is a linear change. Here $d\Delta V_g/d\text{time}$ is roughly 6.5 mV/min. During the linear region there are many available sites for the protein to bind to. The proteins are not competing for a site. After the linear region there is a nonlinear region that gradually reaches a horizontal line where there is no change in ΔV_g . In this region the surface is becoming saturated and proteins are competing for binding sites. Once the surface is entirely saturated there is no change in ΔV_g .

Since the PLL has such a large affinity of binding to the SiO₂ surface, much of the PLL stays bond to it permanently. Because of this there is a shift in the transistor curve from before to after the PLL is delivered. This shift in gate voltage can be seen in Figure 3.8.

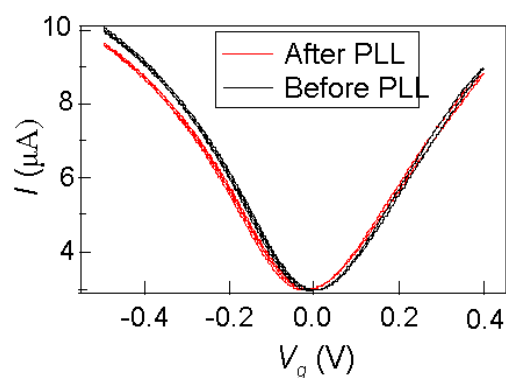


Fig. 3.8 Before introduction of PLL and after introduction of PLL transistor curve. There is a shift in the curve of about 15 mV due to the presence of PLL on the graphene of the device.

Similar experiments have been performed on CNT FET biosensors and a comparison of CNT devices with graphene devices is warranted. Leyden et. al. used PLL and a PBS buffer with a very similar flow rate. The right image in Figure 3.9 shows the results they obtained from a 4 nM PLL solution.

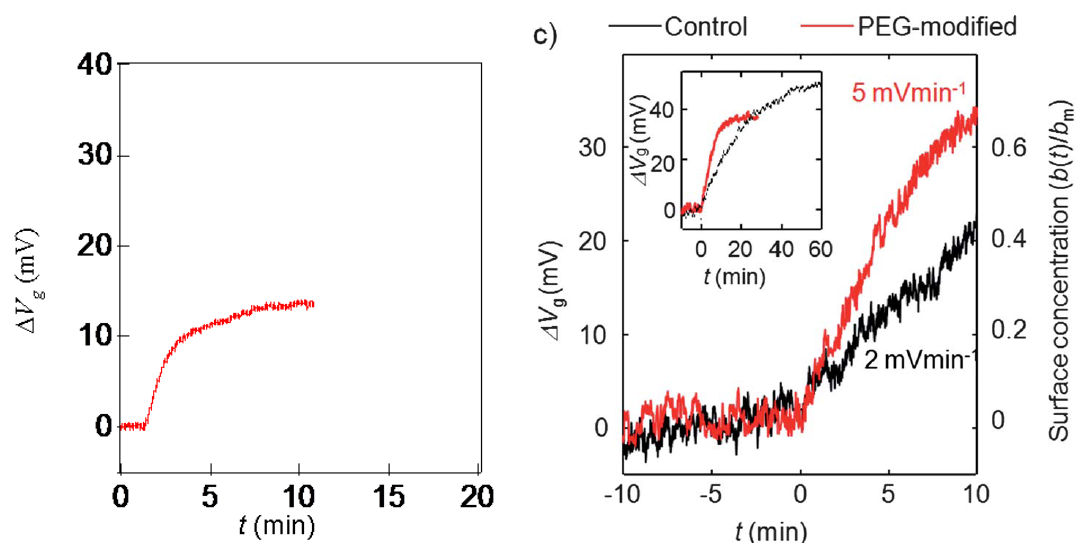


Fig. 3.9 Comparison of noise levels for a graphene device and a CNT device. The left image is Figure 3.7 but with different axis scales to show a comparison to a CNT device on the right. The right image is data taken from Leyden et. al.¹³ Notice the noise level of the two devices and how the graphene device is much quieter.

The left image in Figure 3.9 is the same data as Figure 3.7 but with the axis scaled differently so that a comparison can be made to the Leyden data. Notice the noise level of the two sets of data. The graphene data (left) is much quieter than the CNT device (right). We note that the overall signal is also smaller on the graphene device, however, we believe PLL binding to the graphene surface saturates at a lower surface concentration compared to the SiO₂ surface. Further experiments are needed to quantify the relative surface concentrations of PLL on graphene versus PLL on SiO₂.

Regardless of PLL affinity for graphene, we are encouraged by the low noise seen in Figure 3.9. In the upcoming sections we focus on experiments where an aptamer is introduced to enhance binding to the graphene surface.

3.4 Thrombin Modified Graphene Device

The PLL experiment is encouraging but is not biologically specific. Any positively charge protein will stick to the surface. Because of this, aptamer modified graphene devices were tested. With the aptamer modified devices it is possible to have protein specific biosensors.

A process inspired by Ohno et. al. was used to attach the aptamer to the graphene.¹⁴ Thrombin specific synthesized oligonucleotide DNA aptamers were obtained from Integrated DNA Technologies and the base sequence was 5'-5 Amino C6/GGT TGG TGT GGT TGG-3'. To immobilize the aptamer onto the graphene a linker molecule was needed between the aptamer and graphene. Amine-reactive 1-pyrenebutanoic acid succinimidyl ester (PBASE) was obtained from Invitrogen and provided the linker between the aptamer and graphene. The PBASE binds to the graphene surface via a π stacking mechanism. The oligonucleotide was synthesized with an amine group which reacts with the amine-reactive PBASE molecule resulting in a bond between the PBASE and aptamer.

The G-FET was soaked in a methanol solution with 5 mM PBASE for 1 hour at room temperature. The device was then rinsed with methanol and placed in a bath of 20 mM 2-morpholinoethanesulfonic acid (MES) with 1 nM solution of thrombin

aptamer. It was allowed to soak in the aptamer bath for 12 hours at room temperature. After the aptamer bath, a rinse with MES solution was performed to remove any excess PBASE and aptamer from the surface. Thrombin from human plasma was obtained from Sigma-Aldrich.

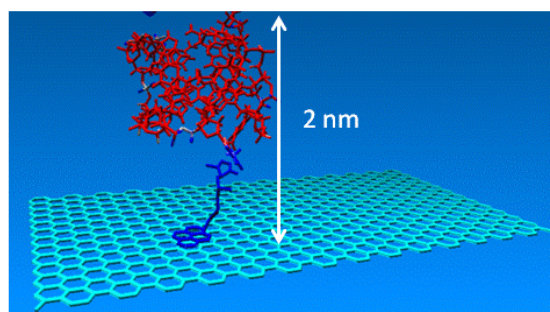


Fig. 3.10 Cartoon of PBASE bound to graphene and thrombin aptamer bound to PBASE

Figure 3.11 is an atomic force microscope (AFM) image of the graphene before and after the modification of aptamer was applied. The apparent height of the

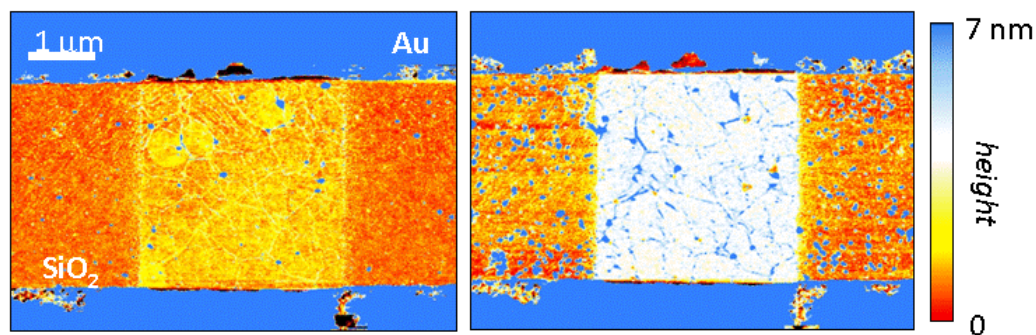


Fig. 3.11 AFM images of before (left) and after (right) aptamer modification of graphene. A height difference of approximately 2 nm was measured indicating that the graphene sheet had aptamer attached to it.

graphene, relative to the SiO₂ substrate, increased by 2 nm after the aptamer modification. This is indicative of aptamer being immobilized on the surface of the graphene. In the AFM figure the blue area at the top and bottom are the gold electrodes, the red area is the SiO₂ substrate, the yellow area in the left image is the graphene ribbon, and the white area in the right image is the aptamer modified graphene. The graphene ribbon is approximately 3.5 μm wide and the distance between the electrodes is 4 μm.

Figure 3.12 shows the transistor curve for this device (left). The Dirac point to the right indicates that the device is more p-type as opposed to the device in Figure 3.1 which has almost no doping. The other two graphs in Figure 3.12 are from two other devices showing once again the consistency of devices. All devices that were modified with aptamer showed a Dirac point near 0.3 V. All devices that were not aptamer modified showed a Dirac point near 0 V. This p-type doping of aptamer modified G-FET is likely due to the aptamer being negatively charged.

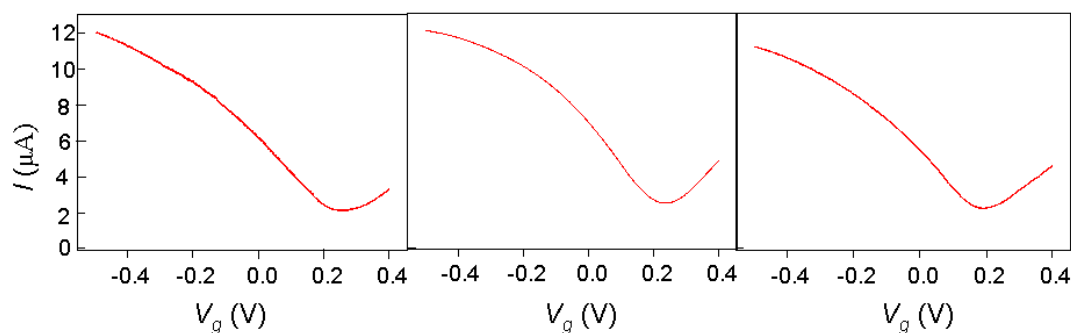


Fig. 3.12 Transistor curves for three different devices with aptamer modified graphene. Again there is consistency from device to device. The Dirac point to the right is because of the p-type doping from the negatively charged aptamer being attached to the graphene.

The flow lines were flushed with ethanol and then 1 mM MES buffer. The flow cell and PDMS stamp were flushed with DI water and then with 1 mM MES buffer. Four different concentrations of thrombin solutions were prepared in 1 mM MES buffer; 10 nM, 30 nM, 100 nM, and 300 nM. Figure 3.13 shows the real time response as the sensor was challenged with thrombin solution. The sensor was rinsed with buffer between each thrombin solution. As explained in section 3.2, $I(t)$ was converted to $\Delta V_g(t)$.

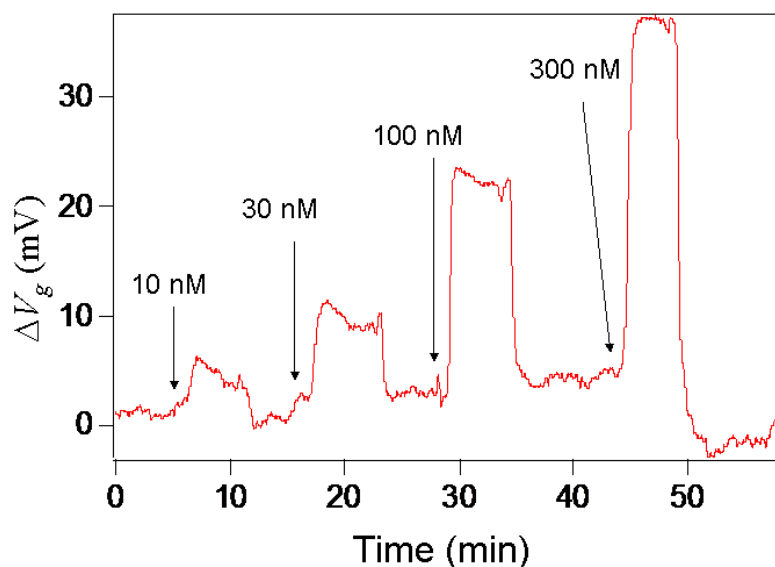


Fig. 3.13 Real time data of thrombin experiment. When thrombin binds to the aptamer there is a change in the effective gate voltage. At different concentrations there are different changes in the effective gate voltage due to the amount of thrombin that is bound to the aptamer. Data was filtered by hardware at 3 kHz. Sampling was done at 2 Hz.

The binding between the thrombin and the thrombin aptamer is a dynamic binding. There is a low affinity between the protein and aptamer, so there is a constant binding and unbinding between the two. This is measured by a dissociation constant (K_d). The dissociation constant is a ratio of the concentration of two analyte separate

over the concentration of two analyte bound together, the higher the affinity of the bond the lower the dissociation constant.

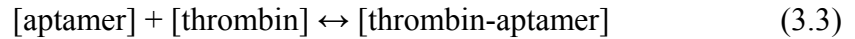


$$K_d = \frac{[A][B]}{[AB]} \quad (3.2)$$

Reported K_d values for this aptamer and protein range from 3-450 nM.^{19,20,21,22,23} This large discrepancy is attributed to different experimental methods and conditions, and the composition and pH of the incubation buffer.^{21,22,23}

For this experiment the four different solutions of thrombin were introduced at different times. For different concentrations of thrombin there should be a different shift in the effective gate voltage, because depending on how much thrombin is available, there will be differing amounts bound to the surface. The higher the concentration of protein available the more protein there will be bound to the surface at a given time, that is until there are no available binding sites left. Hence there is a maximum change in effective gate voltage, when the surface is saturated. Between each of the solutions the MES buffer was flowed. When the buffer is introduced without any protein, all of the protein bound to the aptamer is removed and none is replaced. This is because as protein that is bound to the aptamer dissociates, if only buffer is present, there is no protein present to replace the protein that has left, hence, over a short period of time there will be no protein left on the surface. This is the reasoning behind flowing buffer after each concentration of thrombin is introduced.

This data shown in Figure 3.13 convincingly demonstrates reversible binding. From this data a dissociation constant can be extracted. The interaction between aptamer and thrombin can be described:



which leads to the relation between the change in effective gate voltage (ΔV_g) and the thrombin concentration:

$$\Delta V_g = \Delta V_{g \max} \left(\frac{[\text{thrombin}]}{[\text{thrombin}] + K_d} \right) \quad (3.4)$$

where K_d is the dissociation constant and $\Delta V_{g \max}$ is the max change in effective gate voltage possible.^{14,24} Figure 3.14 shows the change in effective gate voltage vs. thrombin concentration. The solid line is fit using equation 3.4, the Langmuir equation, where $\Delta V_{g \max}$ and K_d are fit parameters. Values found with this fit were $K_d = 134 \pm 15$ nM and $\Delta V_{g \max} = 53 \pm 3$ mV. This K_d value falls within the 3-450 nM range presented earlier.

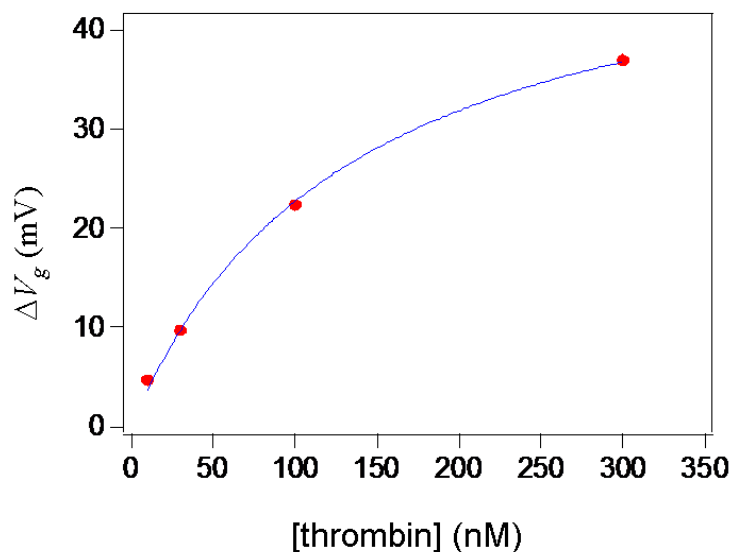


Fig. 3.14 Red dots are real data of change in effective gate voltage vs. thrombin concentration. Solid blue line is fit using eq. # with $\Delta V_{g\max} = 53 \pm 3$ mV and $K_d = 134 \pm 15$ nM.

To show that the device is specific to thrombin a competing protein was introduced. Figure 3.15 is current vs. time of data from Figure 3.13 and when 100 nM of streptavidin is introduced to the system.

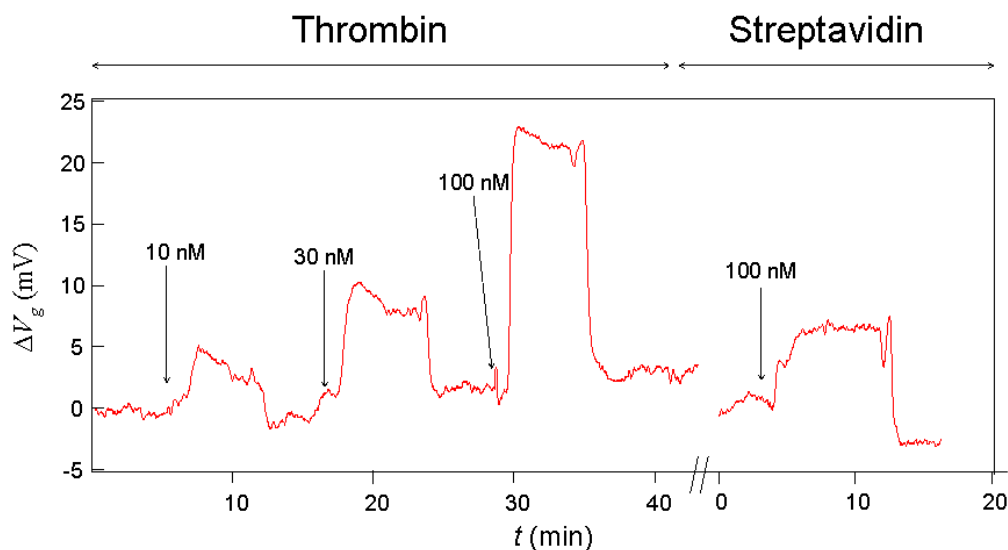


Fig. 3.15 Time data of aptamer modified graphene device with the introduction of competing protein, 100 nM Streptavidin in MES buffer. The Streptavidin gives a signal but it is compared to the signal of the different concentrations of thrombin and is similar to the signal given by 10 nM of thrombin. Data was filtered by hardware at 3 kHz. Sampling was done at 2 Hz.

Initially, an MES buffer is flowed then at 1 minute streptavidin is introduced. There is a 100 μ A change in current. Then at 9 minutes the MES buffer is reintroduced.

Although there is a change in current from the streptavidin, it is comparable to the signal as 10 times less thrombin (Figure 3.15 left).

Chapter 4

Conclusion

Disadvantages of commercially available biosensors were discussed. Surface plasmon resonance biosensors are very expensive (\$100,000), Fluorescence based biosensors take several hours and a trained technician to get results, and QCM require very high current stability to obtain accurate results. Graphene field-effect transistor biosensors can address these shortcomings.

Using previous experimental work and an analysis of noise properties of CNTs and graphene, we showed that at CNT growth densities of 5 CNTs/ μm or less, graphene has a lower noise value. Because it is difficult to grow higher than 3 CNTs/ μm , graphene was chosen for further study. We experimentally confirmed that CVD graphene device have a similar noise floor to devices made from mechanically exfoliated graphene.

Results from two different biosensing experiments were presented. First, we demonstrated that the G-FET device is able to sense the PLL protein binding. Second, thrombin sensing experiment with aptamer modified graphene was conducted. The G-FET device was able to sense the presence of thrombin bound to the aptamer. Different concentrations of thrombin were introduced and the current response changed with the introduction of the different concentrations. This indicated that the thrombin was binding to the aptamer that was immobilized on the graphene surface. The device was challenged with a competing protein. A 100 nM solution of streptavidin was introduced and it gave the same signal as a 10 nM solution of

thrombin. This suggests that the device can be used to sense a specific protein. In conclusion, a protein specific device was fabricated and tested, and showed that it had specificity. This improvement opens the door to use of CVD graphene in FET devices as protein specific biosensors.

Bibliography

1. Collings, A. F. & Caruso, F. Biosensors: recent advances. *Reports on Progress in Physics* **60**, 1397–1445 (1997).
2. Pejčić, B., Marco, R. D. & Parkinson, G. The role of biosensors in the detection of emerging infectious diseases. *The Analyst* **131**, 1079 (2006).
3. Homola, J. Present and future of surface plasmon resonance biosensors. *Anal Bioanal Chem* **377**, 528–539 (2003).
4. Rissin, D. M. *et al.* Single-molecule enzyme-linked immunosorbent assay detects serum proteins at subfemtomolar concentrations. *Nat. Biotechnol.* **28**, 595–599 (2010).
5. Moerner, W. E. & Fromm, D. P. Methods of single-molecule fluorescence spectroscopy and microscopy. *Review of Scientific Instruments* **74**, 3597–3619 (2003).
6. Ziegler, C. *et al.* Bioelectronic noses: a status report. Part III Co-ordinating authors: Ch. Ziegler and W. Göpel. All other authors are contributing authors. 1. *Biosensors and Bioelectronics* **13**, 539–571 (1998).
7. Buchtip, S. *et al.* Detection of the shrimp pathogenic bacteria, *Vibrio harveyi*, by a quartz crystal microbalance-specific antibody based sensor. *Sensors and Actuators B: Chemical* **145**, 259–264 (2010).
8. Eichelbaum, F., Borngraber, R., Schroder, J., Lucklum, R. & Hauptmann, P. Interface circuits for quartz-crystal-microbalance sensors. *Review of Scientific Instruments* **70**, 2537–2545 (1999).
9. Miroslav Pohanka & Skládal, P. Electrochemical biosensors – principles and applications. *Journal of APPLIED BIOMEDICINE* **6**, 57–64 (2008).
10. Tight Binding Calculation of Molecules and Solids. *Physical Properties Of Carbon Nanotubes* 17–33 (1998).
11. Ashcroft, N. W. & Mermin, N. D. *Solid state physics*. (Saunders College: 1976).
12. Sutton, A. P. *Electronic Structure of Materials*. (Oxford University Press, USA: 1993).
13. Leyden, M. R. *et al.* Increasing the detection speed of an all-electronic real-time biosensor. *Lab on a Chip* **12**, 954 (2012).
14. Ohno, Y., Maehashi, K. & Matsumoto, K. Label-free biosensors based on aptamer-modified graphene field-effect transistors. *J. Am. Chem. Soc.* **132**, 18012–18013 (2010).
15. Mannik, J., Heller, I., Janssens, A. M., Lemay, S. G. & Dekker, C. Charge Noise in Liquid-Gated Single-Wall Carbon Nanotube Transistors. *Nano Lett.* **8**, 685–688 (2008).
16. Heller, I. *et al.* Charge Noise in Graphene Transistors. *Nano Lett.* **10**, 1563–1567 (2010).
17. Artyukhin, A. B. *et al.* Controlled electrostatic gating of carbon nanotube FET devices. *Nano Lett.* **6**, 2080–2085 (2006).
18. Leyden, M. R. *et al.* Increasing the detection speed of an all-electronic real-

- time biosensor. *Lab on a Chip* **12**, 954 (2012).
19. Wu, Q., Tsiang, M. & Sadler, J. E. Localization of the single-stranded DNA binding site in the thrombin anion-binding exosite. *J. Biol. Chem.* **267**, 24408–24412 (1992).
 20. Tasset, D. M., Kubik, M. F. & Steiner, W. Oligonucleotide inhibitors of human thrombin that bind distinct epitopes. *J. Mol. Biol.* **272**, 688–698 (1997).
 21. German, I., Buchanan, D. D. & Kennedy, R. T. Aptamers as ligands in affinity probe capillary electrophoresis. *Anal. Chem.* **70**, 4540–4545 (1998).
 22. Li, J. J., Fang, X. & Tan, W. Molecular aptamer beacons for real-time protein recognition. *Biochem. Biophys. Res. Commun.* **292**, 31–40 (2002).
 23. Berezovski, M., Nutiu, R., Li, Y. & Krylov, S. N. Affinity analysis of a protein-aptamer complex using nonequilibrium capillary electrophoresis of equilibrium mixtures. *Anal. Chem.* **75**, 1382–1386 (2003).
 24. Zhu, H., Suter, J. D., White, I. M. & Fan, X. Aptamer Based Microsphere Biosensor for Thrombin Detection. *Sensors* **6**, 785–795 (2006).

